1   **Coexistence and coupling of ferroelectricity and magnetism**

2   **in an oxide two-dimensional electron gas**

3

4   Julien Bréhin[1], Yu Chen[2], Maria D'Antuono[2,3], Sara Varotto[1], Daniela Stornaiuolo[2,3], Cinthia

5   Piamonteze[4], Julien Varignon[5], Marco Salluzzo[2§] and Manuel Bibes[1]*

6

7   [1] Unité Mixte de Physique, CNRS, Thales, Université Paris Saclay, 91767 Palaiseau, France

8   [2] CNR-SPIN, Complesso Monte S. Angelo - Via Cinthia, 80126 Napoli, Italy

9   [3] University of Naples "Federico II", Complesso Monte S. Angelo - Via Cinthia, 80126 Napoli, Italy

10   [4] Swiss Light Source, Paul Scherrer Institut, 5232 Villigen PSI, Switzerland

11   [5] CRISMAT, CNRS UMR 6508, ENSICAEN, Normandie Université, 6 boulevard Maréchal Juin, 14050

12   Caen Cedex 4, France

13

14

15   **Multiferroics are compounds in which at least two ferroic orders coexist – typically**

16   **(anti)ferromagnetism and ferroelectricity[1] – and whose investigation has been a major area of**

17   **materials science during the last two decades. While magnetic order can arise in both insulating and**

18   **metallic compounds, ferroelectricity is in principle only allowed in insulators, although ferroelectric**

19   **metals were proposed over 60 years ago[2]. Recently, several two-dimensional systems have been**

20   **reported to behave as ferroelectric metals[3–5]. Yet, their combination with magnetic order remains**

21   **elusive. Here, we show the coexistence of ferroelectricity and magnetism in an oxide-based two-**

22   **dimensional electron gas (2DEG). Ti-$L_{3,2}$ edge X-ray linear dichroism data evidences a modulation of**

23   **the Ti-O polar displacements depending on the ferroelectric polarization direction while transport**

24   **data reveal a voltage-induced hysteresis of the sheet resistance, reminiscent of the ferroelectric**

25   **polarization loop. The 2DEGs displays anomalous Hall effect and magnetoresistance that can both**

26   **be modulated and cycled by switching the remanent polarization, demonstrating a magnetoelectric**

27   **coupling. Our findings provide new opportunities in quantum matter stemming from the interplay**

28   **between ferroelectricity, ferromagnetism, metallicity and Rashba spin-orbit coupling.**

29   § marco.salluzzo@spin.cnr.it

30   * manuel.bibes@cnrs-thales.fr

31   Nearly 70 years ago, Anderson and Blount introduced the concept of ferroelectric metals[2] in which

32   ferroelectricity and conductivity coexist in the same phase, which *a priori* seems physically impossible

33   because itinerant electrons screen electrostatic forces between ions. More recently, $LiOsO_3$ was

34   confirmed as the first unambiguous ferroelectric-like metal[6] and ferroelectricity was later evidenced

35   in flakes of conducting WTe_2[3,4]. Another approach to generate a ferroelectric metal is based on the

36   introduction of charge carriers in a bulk ferroelectric such as $BaTiO_3$[7] or Ca-substituted $SrTiO_3$[8] (Ca-

37   STO). Signatures of the structural transitions associated with the ferroelectric character are then visible

38   in the temperature dependence of the resistivity, but in these materials the ferroelectric polarization

39   cannot be switched. This research however inspired a related strategy aiming at the generation of a

40   two-dimensional electron gas (2DEG) at the surface of these compounds[5], confining the charge carriers

41   and thus the metallic region over a few unit cells near the surface, the rest of the ferroelectric material

42   remaining insulating. Structural and electrostatic coupling between the insulating part and the metallic

43   part in the ferroelectric is then harnessed to introduce switchable dipoles in the metal, thereby

44   achieving a ferroelectric 2DEG.

45   While ferroelectric-like 2DEGs display novel functionalities such as the non-volatile control of spin-

46   charge conversion[9], to date, the ferroelectric character of the 2DEG itself has not been unambiguously

47   proven. In addition, the introduction of magnetism into ferroelectric metals – leading to the generation

48   of multiferroic metals that would open vast perspectives for spin-orbitronics[10,11] – remains elusive.

49   In this paper, we merge the fields of multiferroics[1] and oxide interfaces[12] by incorporating

50   ferroelectricity and magnetism into a 2DEG based on $SrTiO_3$ (STO). Our work echoes research on 2D

51   van der Waals materials in which ferroelectricity[13,14], ferromagnetism[15,16] and, most recently,

52   multiferroicity[17] were introduced, albeit in this latter case while keeping the material insulating. Our

53   design strategy, sketched in Fig. 1a, circumvents the daunting challenge to stabilize ferromagnetism,

54   ferroelectric and metallicity in a single 2D material. We propose to insert a magnetic $EuTiO_3$ (ETO) layer

55   between $LaAlO_3$ (LAO) and STO to induce magnetism in the 2DEG (bottom left) and to replace STO by

56   ferroelectric Ca-STO to make the 2DEG behave as a ferroelectric metal (top right). Thereby, we

57   simultaneously induce magnetism and ferroelectricity to achieve a multiferroic 2DEG (MF-2DEG;

58   bottom right) in which magnetism and spin-dependent transport can be controlled by ferroelectricity.

59   To support our design strategy, we performed density functional theory (DFT) simulations. We

60   modelled (001) slabs of the form $(STO)_{12}/(ETO)_2/(LAO)_6$/vacuum with an AlO_2 termination and imposing

61   a ferromagnetic arrangement for Eu^{2+} cations (see Fig. 1b for a sketch of the system). Previous DFT

62   calculations on metallic ETO-based heterostructures suggest that the ground state is ferromagnetic[18]

63   in agreement with experimental studies[19]. In order to mimic the ferroelectric behaviour of Ca-STO, we

64 applied a compressive strain of 1.6% to STO inducing a polarization along the (001) direction. Then we

65 locked the STO atomic positions of the first four unit-cells in our slabs and considered two cases with

66 either the polarization pointing toward (P_{up}) or away from (P_{dn}) the interface. We obtain a n-type

67 electron gas at the interface between STO/ETO and LAO as inferred by the projected density of states

68 (PDOS) on the upper TiO_2 layers reported in Fig. 1c and d. In our calculations the 2DEG thus appears as

69 a consequence of a polar catastrophe[20] although we cannot exclude that oxygen vacancies may also

70 contribute[21]. The DOS at the Fermi level is sizeable for P_{up} and smaller but finite for P_{dn}.

71
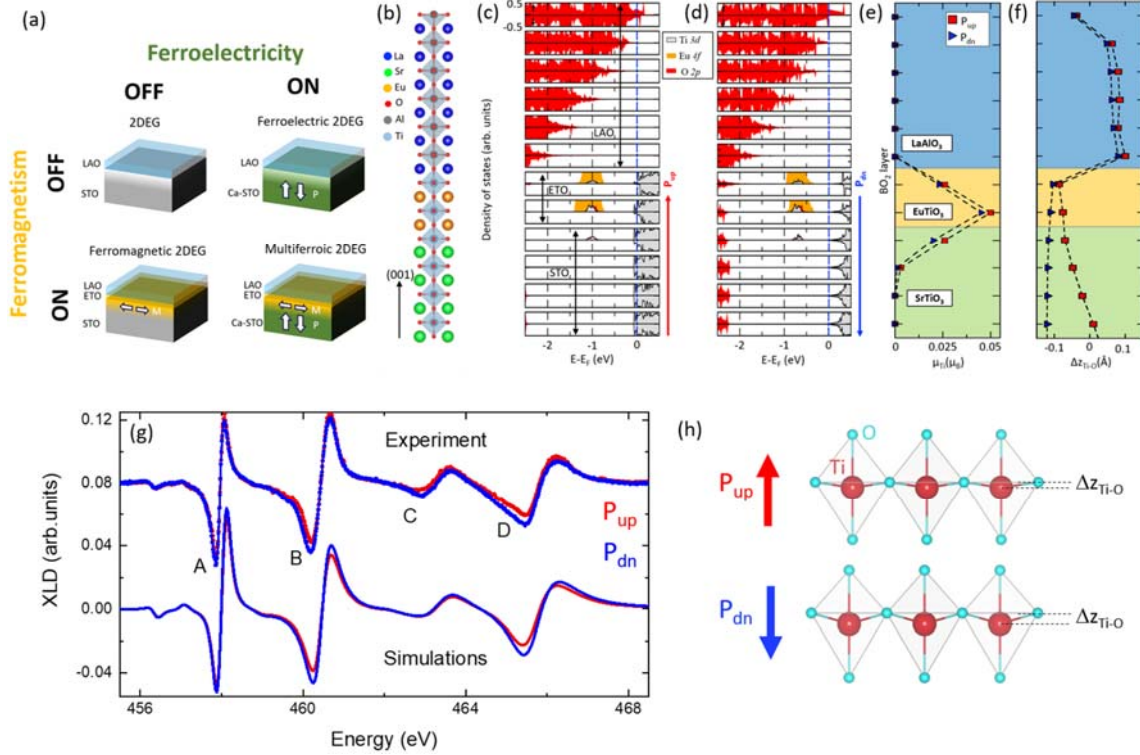
72 **Fig. 1. Design of a multiferroic 2DEG.** *(a) Starting from the non-magnetic, non-ferroelectric interface*

73 *system LAO/STO (top left), ferroelectricity can be introduced by replacing STO by Ca-STO (top right).*

74 *Ferromagnetism can be introduced by inserting a few unit cells of ETO between LAO and STO (bottom*

75 *left). Combining both approaches yields a multiferroic 2DEG (bottom right). (b) Sketch of the slab*

76 *configuration tested in the electronic structure simulations. (c) and (d) Layer-decomposed projected*

77 *density of states on O 2p and Ti d states as a function of a polarization pointing toward (c) and outward*

78 *(d) the interface. Positive and negative values stand for spin up and spin down, respectively. The Fermi*

79 *level is set at 0 eV and is represented by the blue dashed line. (e) Computed magnetic moments on Ti*

80 *cations for the two polar states. (f) Relative displacement of the B cation with respect to oxygen ions*

81 *along the growth direction. (g) X-ray linear dichroism spectra at the Ti $L_{3,2}$ edge measured at 2 K and*

82 *ferroelectric remanence for P_{up} and P_{dn} on a LAO/ETO//Ca-STO sample (top) and atomic multiplet*

83 *simulations (bottom). (h) Sketches of the TiO$_6$ octahedra configurations corresponding to the*

84 *simulations in (g), evidencing different off-centered Ti-O displacements Δz_{Ti-O} for P$_{up}$ and P$_{dn}$, consistent*

85 *with the DFT calculations.*

86 Due to the presence of the ferromagnetically ordered Eu^{2+} spins, Ti cations experience a spin-

87 dependent potential which produces asymmetries between spin-up and spin-down channels for the

88 *d*-states. It results in a spin-polarized DOS and a net magnetic moment on Ti cations that spreads over

89 four TiO$_2$ layers in the STO below the ETO/LAO interface. As visible in Fig. 1e, the Ti magnetic moment

90 is maximum for the layer sandwiched between two Eu^{2+} layers below the interface with LAO, but

91 extends into the first STO unit-cells.

92 Fig. 1f displays the relative displacement of the Al/Ti (B-cation) and oxygen ions along the growth

93 direction across the structure. In LAO, the displacements are finite and large, due to the electric field

94 created by the polar interface with ETO, but they are equivalent for P$_{up}$ and P$_{dn}$, within error bars. In

95 the STO, the polar displacements related to Ti-oxygen rumpling Δz_{Ti-O} are also present but are different

96 depending on the polarization state, as a consequence of ferroelectricity. Far away from the interface

97 the two polarizations and associated polar displacements would be exactly opposite. Near the

98 interface, they are both biased towards negative values due to the electric field related to the 2DEG

99 confinement, due to the polar discontinuity that causes a polar shift of Ti ions by 0.1-0.15 Å in non-

100 ferroelectric LAO/STO[22,23]. Importantly here, in the 2DEG region, Δz_{Ti-O} takes two different values for

101 P$_{up}$ and P$_{dn}$, indicating that the 2DEG possesses two different remanent polarization states. In other

102 words, it is ferroelectric.

103 To confirm this prediction, we measured the X-ray linear dichroism (XLD) at the Ti $L_{3,2}$ edge on a typical

104 sample prepared by growing a LAO(10 uc)/ETO(2 uc) bilayer onto (001)-oriented Ca-STO single crystals

105 using pulsed laser deposition[19] (see Methods and Extended Data Fig. 1 for details). This element-

106 specific technique corresponds to the difference in the X-ray absorption measured with linear vertical

107 or horizontal polarization and probes the local crystal field splitting. The data plotted in Fig. 1g are

108 measured in total electron yield mode (TEY, probing depth ~2 nm) and thus correspond to the

109 interfacial region including ETO and the first atomic planes of STO where the 2DEG is located. The red

110 and blue spectra are collected at 2 K and at electrical remanence after switching the sample *in situ* into

111 the P$_{up}$ and P$_{dn}$ state, respectively. The XLD spectra look similar to previous ones reported in LAO/STO

112 heterostructures[22] but are visibly modulated by the remanent polarization direction, with the main

113 changes seen in features B and D corresponding to the Ti e_g states. Atomic multiplet calculations

114 reproducing the data show that the splitting of the e_g states is 80±5 meV for P$_{dn}$ and 95±5 meV for P$_{up}$,

115 consistent with the larger Δz_{Ti-O} values computed by DFT for P$_{dn}$ compared to P$_{up}$. The corresponding

TiO$_6$ octahedra configurations are sketched in Fig. 1h. These results thus indicate that the positions of the off-centered Ti ions with respect to the oxygens depend on the polarization state, thereby demonstrating the presence of switchable dipoles in the 2DEG and confirming its ferroelectric character. More quantitatively, since in LAO/STO an orbital splitting of the e$_g$ states by 100 meV corresponds to a built-in polarization of $P_{built-in} \approx -7$ µC/cm² (Ref. [22,23]), we can estimate that the spontaneous ferroelectric polarization in the 2DEG is P$_{FE-2DEG} \approx 0.5 \pm 0.1$ µC/cm². The effective total polarization in the 2DEG is then $P_{built-in} + P_{FE-2DEG} \approx -6.5$ µC/cm² in the P$_{up}$ state and $P_{built-in} - P_{FE-2DEG} \approx -7.5$ µC/cm² in the P$_{dn}$ state.

Coming back to our DFT results, an interesting prediction of Fig. 1e is also that the magnetic moments on Ti cations are different for P$_{up}$ and P$_{dn}$. Thus, ferroelectric switching offers a direct control of the magnetization in the MF-2DEG. Our calculations therefore predict that our 2DEGs are not only multiferroic but also magnetoelectric. This fact may originate from the different band bending induced at the STO/ETO and ETO/LAO interfaces for the two polarization states (Fig. 1b and c): P$_{up}$ (P$_{dn}$) brings a positive (negative) contribution to the electric field present at the TiO$_2$-LaO interface thereby increasing (decreasing) the band bending. Consequently, the Fermi level crosses more Ti 3d states and farther away from the interface for P$_{up}$ than for P$_{dn}$ state where it is limited to three TiO$_2$ layers below the interface.
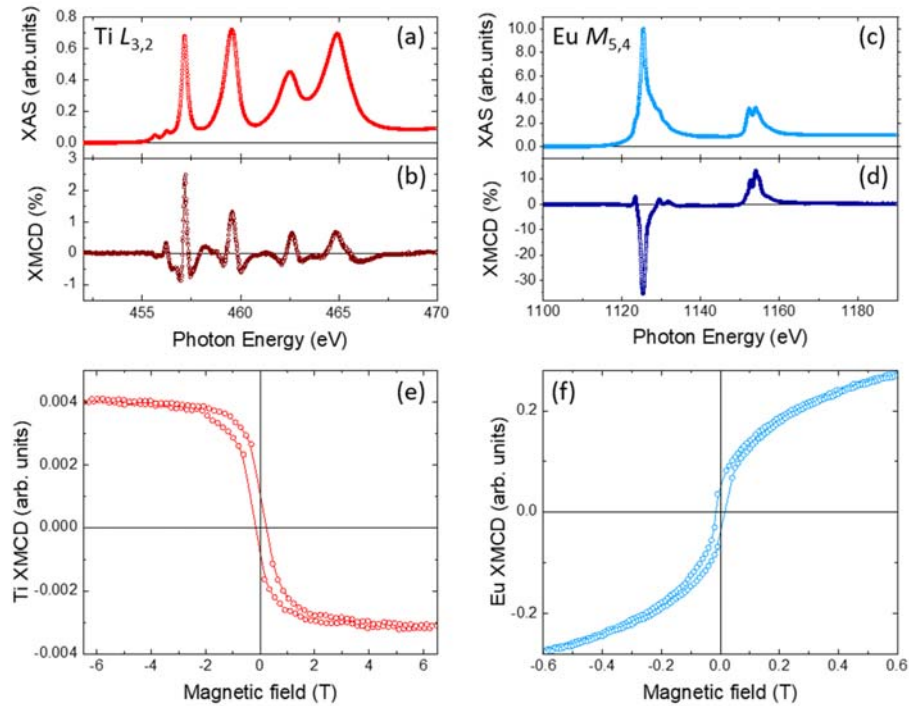

Fig. 2. X-ray absorption spectroscopy and X-ray magnetic circular dichroism. XAS spectra at the Ti L$_{3,2}$ (b) and Eu M$_{5,4}$ edges (c) with corresponding XMCD spectra (b) and (d) for a LAO/ETO//Ca-STO sample,

136 *at 2 K. Magnetic field dependence of the XMCD signal at the Ti $L_{3,2}$ (e) and Eu $M_{5,4}$ (f) edges in grazing*

137 *incidence (in plane magnetic field).*

138 To selectively probe the magnetic response of the elements present in the interface region, we

139 performed further X-ray absorption spectroscopy (XAS) experiments in TEY and measured the X-ray

140 magnetic circular dichroism (XMCD) in an in-plane magnetic field *B*. Fig. 2a-d display XAS and XMCD at

141 5 T for Ti and Eu. The XAS spectrum measured at the Ti $L_{3,2}$ edge (Fig. 2a) is typical of Ti in a valence

142 state close to 4+. A small fraction of Ti^{3+} (a few percent) is however expected to be present owing to

143 the population of the Ti t_{2g} states. Fig. 2b displays the normalized difference between XAS collected

144 with right-and left-circular polarized light, i.e., the XMCD at the Ti $L_{3,2}$ edge. A clear dichroic signal of

145 more than 2% is visible, indicating the presence of Ti magnetic moments in the sample. The shape of

146 the XMCD is reminiscent of that measured in Ref.[19]. Extracting the value of the Ti moment from the

147 XMCD signal is not trivial because sum rules do not apply well to early 3*d* transition metals. However,

148 comparison with Ref.[19] suggests a total moment of around 0.025 μ_B/Ti. Fig. 2e shows the dependence

149 of the XMCD signal at 457.6 eV (corresponding to the Ti L_3 edge) as a function of the in-plane magnetic

150 field: a clear open hysteresis cycle is observed, consistent with a ferromagnetic behaviour probed along

151 an easy magnetization axis. The XAS and XMCD at the Eu $M_{5,4}$ edges are presented in Fig. 2c and 2d.

152 The XAS spectrum is compatible with Eu^{2+}. The large XMCD and the hysteresis loop displayed in Fig. 2f

153 show that ETO is ferromagnetic as in electron-doped ETO[18,24], rather than antiferromagnetic as in the
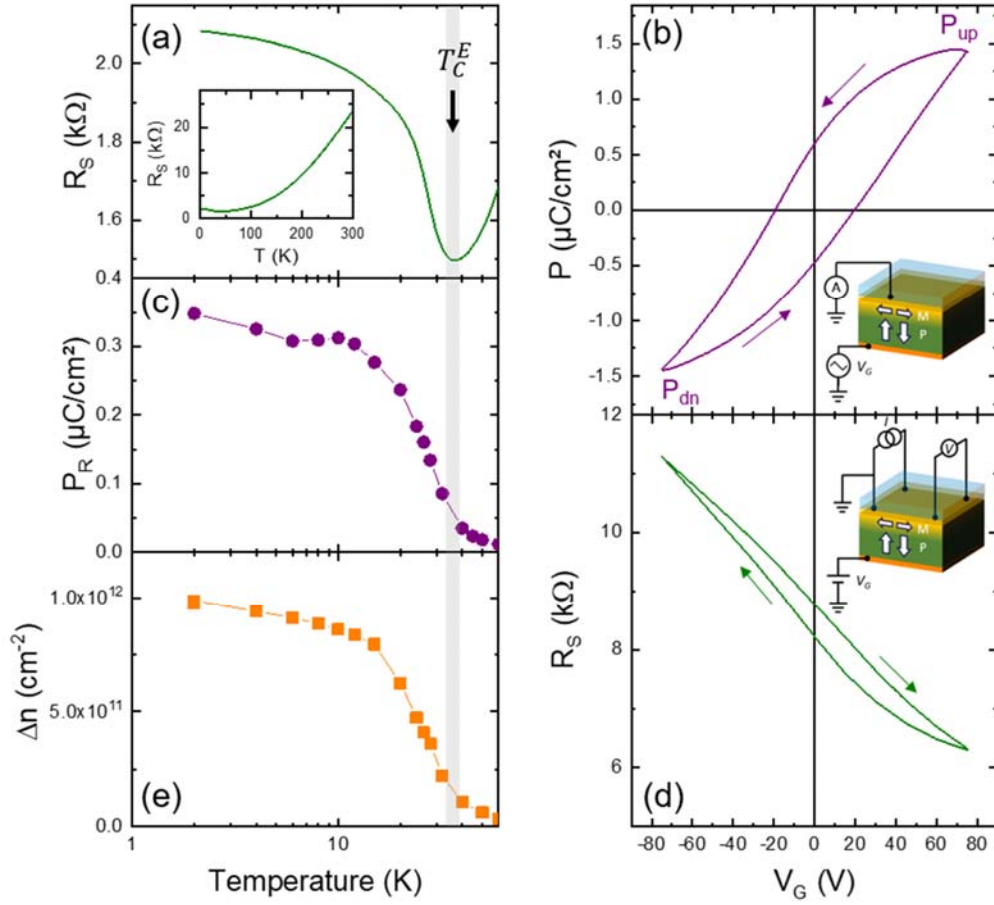
154 bulk[25].

Fig. 3. Ferroelectric and transport properties. *Temperature dependence of the sheet resistance (a). (b) Polarization vs voltage loop at 2 K. (c) Temperature dependence of the remanent polarization. (d) Gate voltage dependence of the 2DEG sheet resistance at 2 K. (e) Temperature dependence of the difference in carrier density between the two ferroelectric polarization remanent states.*

Fig. 3 illustrates the strong coupling between ferroelectricity and transport properties in our MF-2DEGs. As visible on the inset of Fig. 3a, the 2DEG displays the expected metallic temperature dependence of the sheet resistance R_S upon cooling from 300 K. Near 35 K the data however show a minimum below which the resistance increases (Fig. 3a, main panel). This minimum correlates with the transition to the ferroelectric state as observed in electron-doped bulk Ca-STO[8] and in other 2DEGs based on Ca-STO[5]. Fig. 3b presents polarization P vs V_G cycles, which exhibit a clear hysteresis loop (V_G is the gate voltage applied to the structure, see inset), associated with the presence of broad switching peaks in the current (I) *vs* V_G data (see Extended Data Fig. 2). While these loops correspond to the whole Ca-STO, the remanent values are in the range of those estimated in the 2DEG region from XLD data. The P vs V_G cycles remain hysteretic up to 35 K. From the temperature (T) dependence of the remanent polarization (P_R) deduced from remanent polarization cycles (see Extended data Fig. 3)

171   shown in Fig. 3c, we extract a ferroelectric Curie temperature T_C^E of about 35 K, compatible with the

172   T_C^E of 1% Ca-substituted STO[26] and with earlier results on Ca-STO based 2DEGs[5,27].

173   Fig. 3d shows the gate dependence of the sheet resistance: after gate initialization, R_S displays a

174   clockwise hysteretic dependence with the gate voltage that is reproducible upon cycling (Extended

175   Data Fig. 4), a feature absent in equivalent 2DEGs grown on non-ferroelectric STO[28]. R_S is lower when

176   P points towards the 2DEG due to electron accumulation. The data thus indicate that the electronic

177   properties of the 2DEG are strongly modulated by ferroelectricity.

178   The carrier density n extracted from the ordinary Hall effect also depends on the remanent polarization

179   state, n=2.64 10^{13} cm^{-2} for P$_{up}$ and n=2.45 10^{13} cm^{-2} for P$_{dn}$ at 2 K, which yields a difference Δn=~~9.73~~

180   ~~10^{11}~~ cm^{-2}. The dependence of Δn with temperature is shown in Fig. 3e. It vanishes near 35 K, which

181   corresponds to T_C^E, as expected. This ~~Δn corresponds to about 22%~~ of the value of the switched

182   remanent polarization of Ca-STO, i.e., $2P_r/e$=4.38 10^{12} cm^{-2} with P_r=0.35 μC/cm² at 2 K.

183   Although the Hall effect in our 2DEG is mostly linear, closer inspection reveals a nonlinear contribution

184   at low temperature and low magnetic field, ascribed to an anomalous Hall effect (AHE) contribution

185   due to the ferromagnetic order (see Extended Data Fig. 5 and 6). In Fig. 4a and b we plot the AHE at

186   different temperatures for P$_{up}$ and P$_{dn}$. Its shape matches that of XMCD cycles measured with the

187   magnetic field perpendicular to the sample plane (i.e. along the hard magnetization axis), see Extended

188   Data Fig. 7. The AHE amplitude decreases with T and vanishes around 20 K (cf Fig. 4g) which most likely

189   corresponds to the magnetic Curie temperature T_C^M. The AHE is typically higher in the P$_{dn}$ state (Fig.

190   4g) and its shape also depends on the ferroelectric state (see Extended Data Fig. 8). These data thus

191   point to a ferroelectric control of the AHE and thus of the magnetization, which indicates the presence

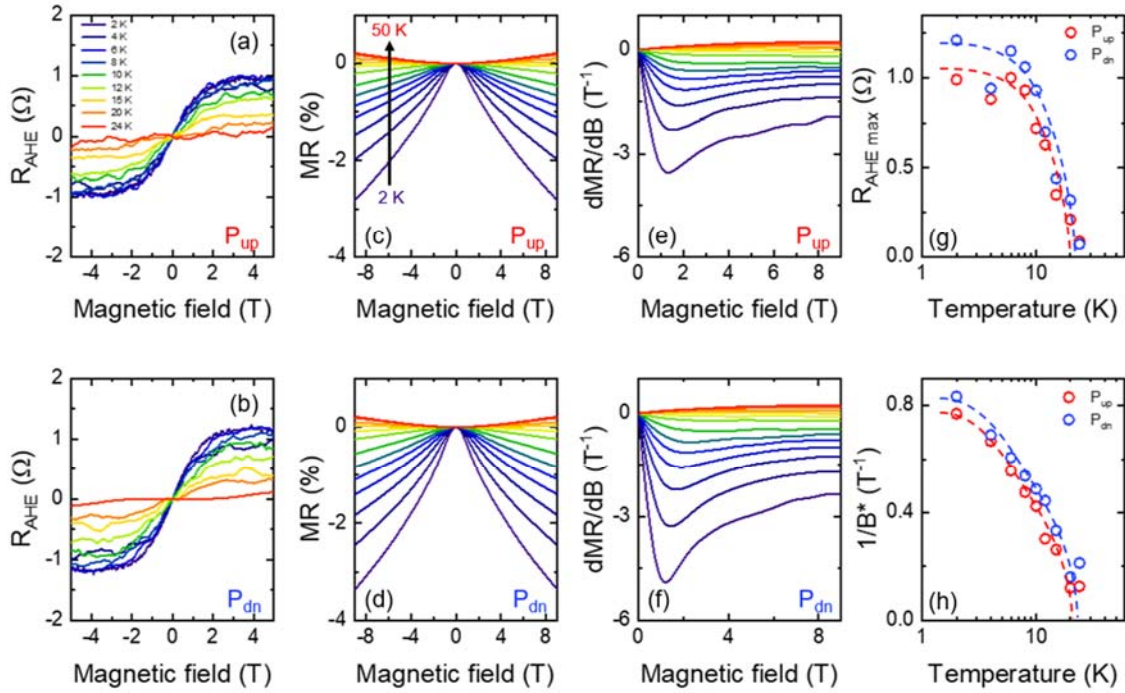192   of a magnetoelectric coupling in our 2DEGs.

193

Fig. 4. Magnetotransport properties for both ferroelectric polarization remanent states. *Anomalous Hall effect at different temperatures for P_{up} (a) and P_{dn} (b). Magnetoresistance (c, d) and its magnetic field derivative (e, f) at different temperatures for P_{up} (c, e) and P_{dn} (d, f). Temperature dependence of the maximum amplitude of the AHE (g) and of the inverse of B* (h) for P_{up} and P_{dn}. In (g) and (h) the dashed lines are guides to the eye.*

Fig. 4c and d show the magnetoresistance (MR) measured with a perpendicular magnetic field as a function of temperature at positive and negative ferroelectric remanence. At high T (e.g. 50 K) the MR shows a small positive quasi-parabolic dependence, typical of Lorentz MR and commonly observed in oxide 2DEGs. The MR scales as $\mu^2 B^2$ with μ the electron mobility, which we estimate to about 70 cm²/Vs at 50 K, in agreement with values deduced from the sheet conductance and carrier density extracted from the ordinary Hall coefficient. As temperature decreases, the MR develops a negative field dependence that resembles what is found in magnetic systems with some degree of spin disorder[29]: as magnetic field increases, spins rotate to align with the external magnetic field, reducing the resistance. The low T MR shows an inflection as a function of magnetic field, which can be better seen from the derivatives (Fig. 4e and f) and is manifested as a pronounced dip at a field B^*. The inflection may signal the approach to saturation of the magnetic lattice. Consistent with this interpretation, the dip in the derivative disappears as T increases. Plotting $1/B^*$ as function of temperature (Fig. 4h) yields a transition temperature that matches the T_C^M deduced from the T dependence of the AHE amplitude (Fig. 4g).

9

214 From the temperature dependence of the R_S vs B data for both ferroelectric remanent states we can

215 plot the electroresistance ER=$(R_{Pup}-R_{Pdn})$ at zero magnetic field and 9 T, see Fig. 5a. The

216 electroresistance decreases with T and vanishes around T_C^E, as expected. Interestingly, ER at 0 T and

217 9 T almost overlap at high temperature but are different below about 20 K, which corresponds to T_C^M.

218 The difference in the ER at 0 T and 9 T corresponds to an electro-magnetoresistance EMR effect

219 (reflecting the influence of the ferroelectric remanent state on the MR, or reciprocally to the influence

220 of magnetic field on the ER). The EMR decreases with increasing temperature and disappears when

221 the first ferroic ordering temperature is reached, here T_C^M. The observation of an EMR effect is

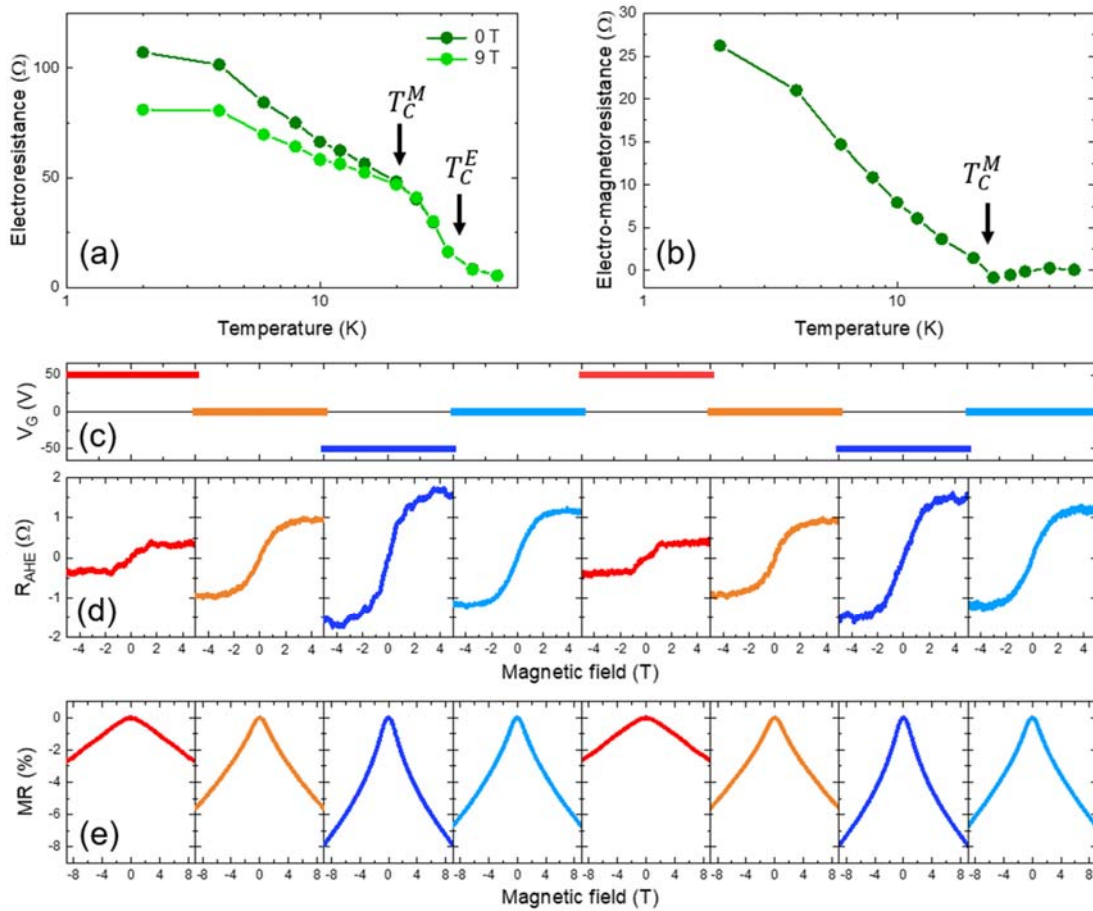222 reminiscent of the behavior found in multiferroic tunnel junctions[30,31].

223

Fig. 5. Magnetoelectric coupling. *(a) Temperature dependence of the electroresistance at 0 and 9 T.*

(b) Temperature dependence of the electro-magnetoresistance. (c) Trains of gate voltages applied to

the samples. Anomalous Hall effect (d) and magnetoresistance (e) measured at 2 K at the voltages

indicated in (c).

228 Fig. 5c-e illustrate the cyclability of the AHE and resistance levels upon setting different polarization

229 states. We have consecutively applied gate voltages of +50 V, 0 V, -50 V and 0 V to respectively pole

230   the ferroelectric upwards, set it in its positive remanent state P_{up}, pole the ferroelectric downwards

231   and set it in its negative remanent state P_{dn} (cf Fig. 5c). For each state we have measured the AHE and

232   the MR, see Fig. 5d and 5e, respectively. Both the AHE and MR increase when going from more positive

233   to more negative polarizations. Remarkably, the variations are reproducible from one cycle to the next,

234   attesting of the robustness of the magnetoelectric coupling.

235   While the multiferroic and magnetoelectric characters of the 2DEG are well supported by the data,

236   some results deserve further investigation. For instance, although our DFT calculations suggest that M

237   in the 2DEG should be higher for P_{up} than for P_{dn}, experimentally we find the AHE amplitude to be

238   stronger for P_{dn} than for P_{up}. These results are not necessarily incompatible since in ETO

239   heterostructures the AHE is known to depend non-monotonically on the saturation magnetization,

240   arising from topological points in the band structure, and even showing a sign change with doping[32].

241   From XLD data, we find that the polarization direction modifies substantially the crystal field splitting,

242   which indicates a non-trivial P-dependence of the electronic band structure, as also suggested by DFT

243   calculations. Another puzzling finding is the high $T_C^M \approx 20$ K, which is higher than T_C^M in strained or

244   doped ETO (peaking around 10 K [24]). The different electronic structure of the ferroelectric 2DEG

245   compared to non-ferroelectric STO 2DEGs or doped ETO[32], as well as enhanced correlations in this low-

246   dimensional system, may collaborate to yield this increase.

247   In summary, we have designed and prepared $LaAlO_3/EuTiO_3//Ca-SrTiO_3$ heterostructures harbouring a

248   two-dimensional electron gas that displays coupled ferroelectricity and magnetism coexisting with a

249   metallic behaviour. Our results not only marry the fields of multiferroics and oxide interfaces but also

250   provides a fascinating new physics playground for non-volatile spin-orbitronics[11] and nonreciprocal

251   physics[10]. They call for further theoretical calculations and experiments to address the interplay of the

252   multiferroic behaviour with Rashba SOC. For instance, because of their intrinsic inversion symmetry

253   breaking, MF-2DEGs are expected to display Rashba-type Dzyaloshinskii-Moriya interaction (DMI)[33]

254   leading to chiral spin textures such as skyrmions[34] which here should be controllable by ferroelectricity.

255

262 SPIN" (Grant No. PRIN 20177SL7HC). DFT calculations took advantages of HPC resources of CRIANN

263 through the projects 2020005 and 2007013 and of CINES through the DARI project A0080911453.

264

265 **AUTHOR CONTRIBUTIONS**

266 MB conceived the study and supervised it with MS. YC and MS prepared the samples, collected the

267 RHEED data and imaged the samples by AFM. Preliminary transport measurements were carried out

268 by DS and MDA. JB performed the complete set of polarisation and magneto-transport measurements

269 with help from SV. The analysis was carried out by JB with the help of MB, SV, DS and MS. CP, MS and

270 JB performed the XAS and XMCD experiment and analysed the data. MS performed the atomic

271 multiplet calculations. JV carried out DFT calculations. MB, MS and JB wrote the paper with inputs from

272 all authors.

273

274 **COMPETING INTERESTS**

275 The authors declare no competing interests.

276

277 **DATA AND MATERIALS AVAILABILITY**

278 The data that support the findings of this study are available from the corresponding authors upon

279 reasonable request.

280

281 **REFERENCES**

282 1. Fiebig, M., Lottermoser, T., Meier, D. & Trassin, M. The evolution of multiferroics. *Nat Rev*
283 *Mater* **1**, 16046 (2016).

284 2. Anderson, P. W. & Blount, E. I. Symmetry Considerations on Martensitic Transformations:
285 Ferroelectric Metals? *Physical Review Letters* **14**, 217–219 (1965).

286 3. Fei, Z. *et al.* Ferroelectric switching of a two-dimensional metal. *Nature* **560**, 336–339 (2018).

287 4. Sharma, P. *et al.* A room-temperature ferroelectric semimetal. *Sci. Adv.* **5**, eaax5080 (2019).

288 5. Bréhin, J. *et al.* Switchable two-dimensional electron gas based on ferroelectric Ca: SrTi O 3.
289 *Phys. Rev. Materials* **4**, 041002 (2020).

290 6. Shi, Y. *et al.* A ferroelectric-like structural transition in a metal. *Nature Mater* **12**, 1024–1027
291 (2013).

292 7. Kolodiazhnyi, T. *et al.* Thermoelectric power, Hall effect, and mobility of *n* -type BaTiO 3.
293 *Phys. Rev. B* **68**, 085205 (2003).

294 8. Rischau, C. W. *et al.* A ferroelectric quantum phase transition inside the superconducting
295 dome of Sr1-xCaxTiO3-δ. *Nature Physics* **13**, 643 (2017).

296 9. Noël, P. *et al.* Non-volatile electric control of spin–charge conversion in a SrTiO3 Rashba
297 system. *Nature* **580**, 483–486 (2020).

298 10. Tokura, Y. & Nagaosa, N. Nonreciprocal responses from non-centrosymmetric quantum
299 materials. *Nat Commun* **9**, 3740 (2018).

300 11. Trier, F. *et al.* Oxide spin-orbitronics: spin–charge interconversion and topological spin
301 textures. *Nat Rev Mater* **7**, 258–274 (2022).

302 12. Hwang, H. Y. *et al.* Emergent phenomena at oxide interfaces. *Nature Mater* **11**, 103–113
303 (2012).

304 13. Vizner Stern, M. *et al.* Interfacial ferroelectricity by van der Waals sliding. *Science* **372**, 1462–
305 1466 (2021).

306 14. Yasuda, K., Wang, X., Watanabe, K., Taniguchi, T. & Jarillo-Herrero, P. Stacking-engineered
307 ferroelectricity in bilayer boron nitride. *Science* **372**, 1458–1462 (2021).

308 15. Gong, C. *et al.* Discovery of intrinsic ferromagnetism in two-dimensional van der Waals
309 crystals. *Nature* **546**, 265–269 (2017).

310 16. Huang, B. *et al.* Layer-dependent ferromagnetism in a van der Waals crystal down to the
311 monolayer limit. *Nature* **546**, 270–273 (2017).

312 17. Song, Q. *et al.* Evidence for a single-layer van der Waals multiferroic. *Nature* **602**, 601–605
313 (2022).

314 18. Gui, Z. & Janotti, A. Carrier-Density-Induced Ferromagnetism in EuTiO 3 Bulk and
315 Heterostructures. *Phys. Rev. Lett.* **123**, 127201 (2019).

316 19. Stornaiuolo, D. *et al.* Tunable spin polarization and superconductivity in engineered oxide
317 interfaces. *Nature Materials* **15**, 278–284 (2016).

318 20.   Nakagawa, N., Hwang, H. Y. & Muller, D. A. Why some interfaces cannot be sharp. *Nature*
319 *Mater* **5**, 204–209 (2006).

320 21.   Yu, L. & Zunger, A. A polarity-induced defect mechanism for conductivity and magnetism at
321 polar–nonpolar oxide interfaces. *Nat Commun* **5**, 5118 (2014).

322 22.   Salluzzo, M. *et al.* Structural and Electronic Reconstructions at the LaAlO3/SrTiO3 Interface.
323 *Advanced Materials* **25**, 2333–2338 (2013).

324 23.   Lee, P. W. *et al.* Hidden lattice instabilities as origin of the conductive interface between
325 insulating LaAlO3 and SrTiO3. *Nat Commun* **7**, 12773 (2016).

326 24.   Katsufuji, T. & Tokura, Y. Transport and magnetic properties of a ferromagnetic metal: Eu 1 −
327 x R x TiO 3. *Phys. Rev. B* **60**, R15021–R15023 (1999).

328 25.   Chien, C.-L., DeBenedetti, S. & Barros, F. D. S. Magnetic properties of EuTiO 3 , Eu 2 TiO 4 ,
329 and Eu 3 Ti 2 O 7. *Phys. Rev. B* **10**, 3913–3922 (1974).

330 26.   Bednorz, J. G. & Müller, K. A. Sr1-xCaxTiO3: An XY Quantum Ferroelectric with Transition to
331 Randomness. *Phys. Rev. Lett.* **52**, 2289–2292 (1984).

332 27.   Tuvia, G. *et al.* Ferroelectric Exchange Bias Affects Interfacial Electronic States. *Adv. Mater.*
333 **32**, 2000216 (2020).

334 28.   Biscaras, J. *et al.* Limit of the electrostatic doping in two-dimensional electron gases of
335 LaXO3(X = Al, Ti)/SrTiO3. *Sci Rep* **4**, 6788 (2015).

336 29.   Tokura, Y. & Tomioka, Y. Colossal magnetoresistive manganites. *Journal of Magnetism and*
337 *Magnetic Materials* **200**, 1 (1999).

338 30.   Gajek, M. *et al.* Tunnel junctions with multiferroic barriers. *Nature Mater* **6**, 296–302 (2007).

339 31.   Garcia, V. *et al.* Ferroelectric Control of Spin Polarization. *Science* **327**, 1106 (2010).

340 32.   Takahashi, K. S. *et al.* Anomalous Hall effect derived from multiple Weyl nodes in high-
341 mobility EuTiO 3 films. *Sci. Adv.* **4**, eaar7880 (2018).

342 33.   Imamura, H., Bruno, P. & Utsumi, Y. Twisted exchange interaction between localized spins
343 embedded in a one- or two-dimensional electron gas with Rashba spin-orbit coupling. *Phys. Rev. B*
344 **69**, 121303 (2004).

345 34.   Fert, A., Reyren, N. & Cros, V. Magnetic skyrmions: advances in physics and potential
346 applications. *Nat Rev Mater* **2**, 17031 (2017).

347 35.   Piamonteze, C. *et al.* X-Treme beamline at SLS: X-ray magnetic circular and linear dichroism at
348 high field and low temperature. *J Synchrotron Rad* **19**, 661–674 (2012).

349 36.   Stavitski, E. The CTM4XAS program for EELS and XAS spectral shape analysis of transition
350 metal L edges. *Micron* **41**, 687–694 (2010).

351 37.   Kresse, G. & Hafner, J. *Ab initio* molecular dynamics for liquid metals. *Phys. Rev. B* **47**, 558–
352 561 (1993).

353 38.   Kresse, G. & Furthmüller, J. Efficiency of ab-initio total energy calculations for metals and
354 semiconductors using a plane-wave basis set. *Computational Materials Science* **6**, 15–50 (1996).

355 39.   Sun, J., Ruzsinszky, A. & Perdew, J. P. Strongly Constrained and Appropriately Normed
356 Semilocal Density Functional. *Phys. Rev. Lett.* **115**, 036402 (2015).

357 40.   Varignon, J., Bibes, M. & Zunger, A. Mott gapping in 3 d A B O 3 perovskites without Mott-
358 Hubbard interelectronic repulsion energy U. *Phys. Rev. B* **100**, 035119 (2019).

359 41.   Paul, A., Sun, J., Perdew, J. P. & Waghmare, U. V. Accuracy of first-principles interatomic
360 interactions and predictions of ferroelectric phase transitions in perovskite oxides: Energy functional
361 and effective Hamiltonian. *Phys. Rev. B* **95**, 054111 (2017).

362 42.   Blöchl, P. E. Projector augmented-wave method. *Phys. Rev. B* **50**, 17953–17979 (1994).

363 43.   Monkhorst, H. J. & Pack, J. D. Special points for Brillouin-zone integrations. *Phys. Rev. B* **13**,
364 5188–5192 (1976).

365

366 **METHODS**

367 **Sample preparation:** LAO(n)/ETO(2)/STO heterostructures were fabricated by pulsed laser deposition

368 (PLD) assisted by Reflection High Energy Electron Diffraction (RHEED) from sintered $Eu_2Ti_2O_7$ and

369 crystalline LAO targets onto TiO_2-terminated (001) $Sr_{0.99}Ca_{0.01}TiO_3$. TiO_2 terminated Ca-STO substrates

370 (from SurfaceNet GmbH) were obtained by etching the as-received single crystals in a buffered

371 hydrofluoric acid solution (pH=5.5) and annealed in flowing O_2 for 2h at 1000 °C. ETO and LAO were

372 sequentially deposited in 8×10^{-5} mbar of O_2 at 720 °C. A Ti(20 nm)/Au(50 nm) bilayer was sputtered at

373 as a bottom electrode the back of the substrate to apply a voltage through the substrate for

374 polarization measurements and gate-dependent magnetotransport.

375 **Electric polarisation measurements.** In these experiments performed with a Radiant Multiferroics II

376 tester, a triangular waveform was applied at a frequency of 10 Hz across the Ca-STO, between the

377 Ti/Au bottom electrode (shown in orange in the sketches of Fig. 3a and 3b) and the 2DEG and the

378 current *I* was measured in real time. Integrating the current with time and normalizing by the sample

379 area yields the polarisation. We used the same principle to obtain the "remanent hysteresis" curves

380 by performing the polarization measurements four times just after applying a preset voltage pulse of

381 different polarities: this allows to subtract the non-switching contribution from the total polarization

382 and thus to reconstruct the four branches of the loop keeping only the remanent (switchable)

383 polarization.

384 **Magnetotransport.** Electrical transport measurements were performed on the samples bonded by Al

385 wires in the van der Pauw configuration in a Quantum Design Dynacool cryostat, using a standard DC

386 technique with a Keithley 2400 Sourcemeter, while the gate voltage was applied with another Keithley

387 2450 Sourcemeter between the bottom electrode and the 2DEG. The sheet resistance was measured

388   in four-wire configuration expect for Fig. 3e. Before being analysed the Hall and MR raw signals were

389   anti-symmetrized and symmetrized with respect to magnetic field, respectively.

390   **XAS, XMCD and XLD.** The experiments were performed on the EPFL/PSI X-Treme beamline at the Swiss

391   Light Source[35]. We have used photon-polarization dependent x-ray absorption spectroscopy (XAS)

392   across the Eu $M_{4,5}$ and the Ti-$L_{2,3}$ edge to probe directly the magnetic and orbital properties of Eu and

393   Ti at the interface. Data were acquired in the total electron yield (TEY) mode, which is sensitive to the

394   interfacial region, i.e. 2 nm from the LAO/ETO interface. The Eu $M_{4,5}$ edge and the Ti $L_{2,3}$ x-ray magnetic

395   circular dichroism (XMCD) spectra were obtained as difference between the average of 8 and 16

396   (respectively) XAS spectra acquired with magnetic field parallel and antiparallel to the photon-helicity

397   vector orientations in a sequence alternating reversal of field and polarization at each spectrum. This

398   procedure ensures the best cancellation of spurious effects. The magnetic field dependent

399   magnetization loops shown in Fig. 2 were obtained by measuring, at each field, the difference between

400   the TEY intensity at the Ti-L_3 and M_5-Eu edge peaks, normalized by the intensity below the absorption

401   edge, obtained with two different helicities (combination of polarization and field direction). The XLD

402   spectra in Fig. 1g were obtained in grazing incidence conditions (x-ray incidence angle of 60 degrees

403   respect the surface normal) at 2 K as the difference between the average of 8 XAS spectra acquired

404   with linear polarization parallel (LV) and almost perpendicular (LH) to the interface. Ferroelectric

405   polarization dependent XLD data were acquired by switching in situ the ferroelectric polarization

406   direction with a back-gate voltage (isolated from the ground), and the 2DEG grounded. To verify the

407   effective switching of the polarization during the experiment, several P vs V loops were acquired before

408   the acquisition of each XLD sequence.

409   **Atomic multiplet scattering simulations** including charge transfer (CT) effects were done using charge

410   transfer ligand field multiplet theory, implemented in the CTM4XAS software[36]. Atomic multiplet

411   simulations in Fig. 3f for Ti^{4+} ions were performed in D4h symmetry and included a charge transfer (CT)

412   term to account for the hybridization between Ti-3d and O-2p states in the TiO$_6$ cluster, i.e. a $3d^0+3d^1\underline{L}$

413   configuration, where $\underline{L}$ indicates an hole in the O-2p band. The CT is included in an Anderson impurity

414   type of model where two parameters are necessary to describe the system: the energy difference

415   between the Ti-$3d$ and the ligand band (called Δ here), and the difference U_{pd}-$\underline{U}_{dd}$ between the core

416   hole potential ($U_{pd)}$ and the Hubbard U value (U_{dd}) for Ti-d electrons. Here we used, Δ=5 eV and U_{pd}-

417    $\underline{U}_{dd}$ = 2eV. Finally, the transfer integrals used were 2 and 1 for b$_1$, a$_1$ (d_{x2-y2}, d_{z2}) and b$_2$, e (d_{xy}, d_{xz}/d_{yz})

418   orbitals, respectively. This choice is commonly used for octahedral or close to octahedral systems and

419   the reasoning behind is that the probability for electron transfer is higher (in this case two times higher)

420   for orbitals pointing in the bond direction, as d_{x2-y2}, d_{z2}. The Slater Integrals were reduced by 90%

421   respect the corrected Hartree-Fock values. The broadening used were 0.1 eV for the Gaussian

422   broadening, to account for the energy resolution, and different Lorentzian broadening for each of the

423   4 peaks of the spectrum, namely half width at half maximum of 0.125 eV, 0.33 eV, 0.55 eV, and 0.7 eV

424   for the four XAS peaks (from the first to the last). In the calculations of the Ti-3d XLD as function of the

425   polarization we changed only the crystal field parameters, which were $10D_q$=2.15, and D_s=-0.020, D_t=-

426   0.000 for P_{up} and D_s=-0.023, D_t=-0.001 for P_{dn}.

427   **First-principles simulations** were performed with Density Functional Theory (DFT) using the VASP

428   package[37,38]. In order to better cancel the spurious self-interactions errors inherent to DFT, we have

429   used the meta-GGA SCAN functional[39] that was previously shown to be suited for capturing the physical

430   properties of transition metal perovskite oxides with a 3d element, even without any U parameter on

431   3d states[40]. The choice of this functional is also appealing since Ti 3d occupancies may vary when

432   moving away to the interface with LAO. While DFT+U method may require different U potential

433   depending on Ti d state occupancy and formal oxidation state – U is a potential acting on a subset of

434   orbitals and correcting delocalization errors—, the SCAN-no-U functional may provide a fair description

435   of the physical effects through the different layers upon adding Ti d electrons as it captures key

436   properties of d^1 titanates[40] and d^0 titanates[41]. Nevertheless, the SCAN functional can sufficiently amend

437   delocalization errors for 4f states and we have added a U potential of 5 eV on Eu 4f states in order to

438   capture the insulating character of $EuTiO_3$ in bulk. It yields a band gap of 0.53 eV and a 4f band just

439   below the Ti 3d states as found in more sophisticated but computationally more demanding hybrid

440   functional DFT[18]. Projector Augmented-Wave (PAW, Ref. [42]) potentials are used with the following

441   valence configurations for the different ions: $4s^2 3d^2$ (Ti), $3s^2 3p^1$ (Al), $4s^2 4p^6 5s^2$ (Sr), $5s^2 5p^6 6s^2 5d^1$ (La),

442     $4s^2 4p^6 5s^2 4f^7$ (Eu), $2s^2 2p^4$ (O). The total energy is converged with a cut-off of 500 eV, accompanied with

443   a 6x6x1 Monkhorst-Pack k-mesh[43]. The slab configuration consists of a $(STO)_{10}/(ETO)_2/(LAO)_6$

444   tricomponent material with 20 Å of vacuum on top in order to avoid interactions between periodic

445   replica of the slabs. In order to mimic the spontaneous polarization of the Ca-STO, we have applied a

446   small compressive strain to STO (1.6%) that yields a polarization of 18 $\mu C.cm^{-2}$. The slab is then

447   initialized with a polar STO and we impose that the first 4 unit cells at the bottom are pinned during

448   the whole calculation while all other atomic positions are optimized until forces acting on each atom

449   are lower than 0.01 eV/ Å. A ferromagnetic order is imposed to Eu^{2+} spins throughout the whole

450   calculations (consistent with the ground state of metallic ETO[18]); no initial spins are imposed on Ti

451   cations.

452

453   **METHODS REFERENCES**

454   33.   Piamonteze, C. *et al.* X-Treme beamline at SLS: X-ray magnetic circular and linear dichroism at
455   high field and low temperature. *J Synchrotron Rad* **19**, 661–674 (2012).

456   34.   Stavitski, E. The CTM4XAS program for EELS and XAS spectral shape analysis of transition metal
457   L edges. *Micron* **41**, 687–694 (2010).

458   35.   Kresse, G. & Hafner, J. *Ab initio* molecular dynamics for liquid metals. *Phys. Rev. B* **47**, 558–561
459   (1993).

460   36.   Kresse, G. & Furthmüller, J. Efficiency of ab-initio total energy calculations for metals and
461   semiconductors using a plane-wave basis set. *Computational Materials Science* **6**, 15–50 (1996).

462   37.   Sun, J., Ruzsinszky, A. & Perdew, J. P. Strongly Constrained and Appropriately Normed
463   Semilocal Density Functional. *Phys. Rev. Lett.* **115**, 036402 (2015).

464   38.   Varignon, J., Bibes, M. & Zunger, A. Mott gapping in 3 d A B O 3 perovskites without Mott-
465   Hubbard interelectronic repulsion energy U. *Phys. Rev. B* **100**, 035119 (2019).

466   39.   Paul, A., Sun, J., Perdew, J. P. & Waghmare, U. V. Accuracy of first-principles interatomic
467   interactions and predictions of ferroelectric phase transitions in perovskite oxides: Energy functional
468   and effective Hamiltonian. *Phys. Rev. B* **95**, 054111 (2017).

469   40.   Blöchl, P. E. Projector augmented-wave method. *Phys. Rev. B* **50**, 17953–17979 (1994).
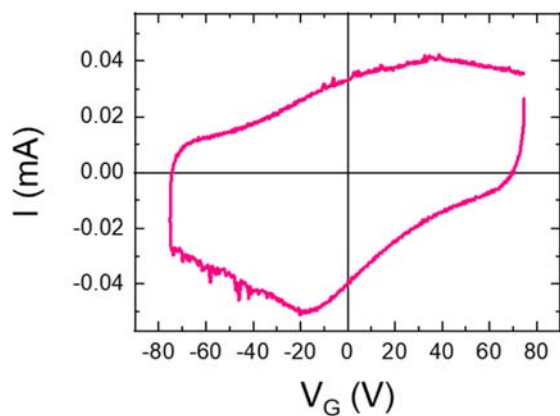
470   41.   Monkhorst, H. J. & Pack, J. D. Special points for Brillouin-zone integrations. *Phys. Rev. B* **13**,
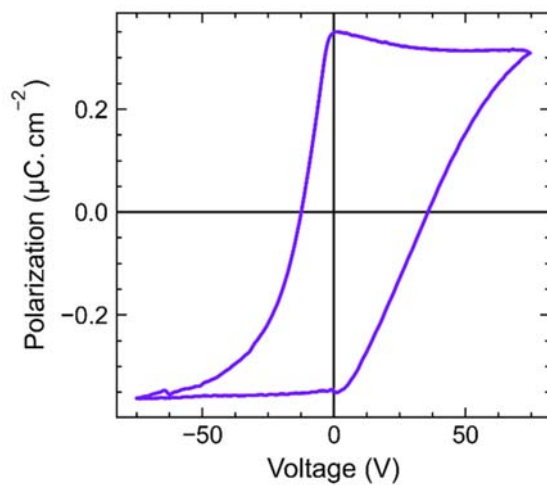471   5188–5192 (1976).

472

474

475
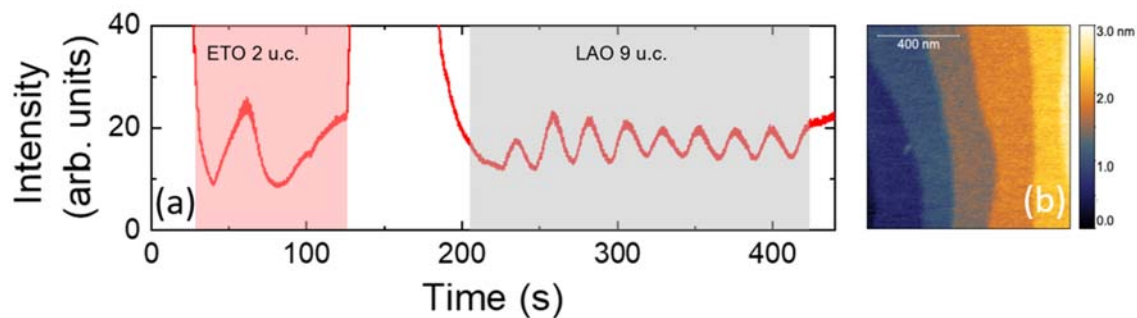
476 **Extended data Fig. 1.** (a) RHEED intensity as function of time during the preparation of a LAO/ETO//Ca-
477 STO heterostructure. (b) AFM image of the sample after growth. Each terrace is separated from its
478 neighbours by a 4 Å high step.

479

480

481 **Extended data Fig. 2.** Current vs voltage loop at 2 K.

482

483 **Extended data Fig. 3.** Remanent polarization loop at 2 K.

19

484
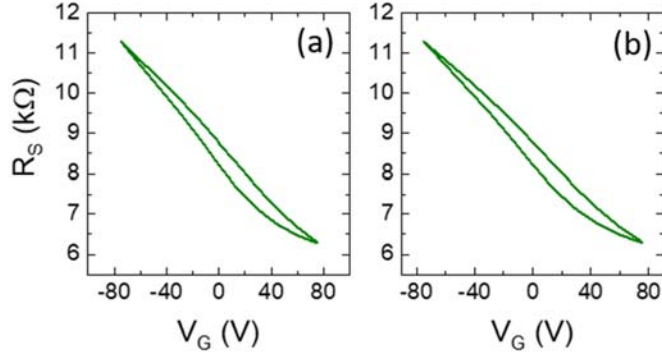
Extended data Fig. 4. Two R vs V_G cycles as in Fig. 3b measured consecutively. They are virtually identical, evidencing that the resistance is modulated by ferroelectricity rather than by irreversible effects occurring on the first cycle in standard STO 2DEGs[28].


488
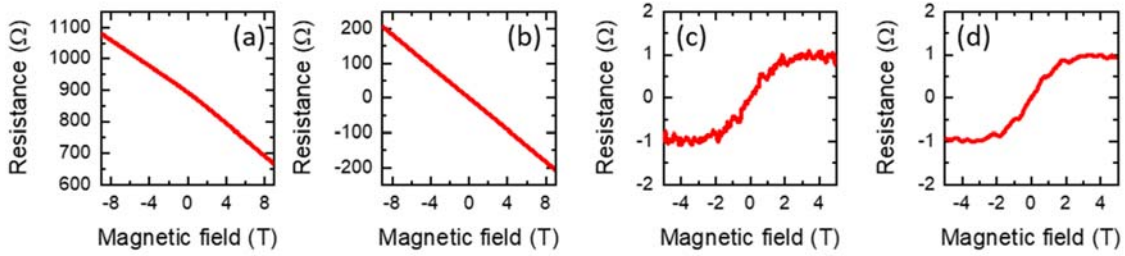
Extended data Fig. 5. (a) Raw transverse resistance measured at 6 K in the P_{up} state. (b) Same data after antisymmetrization. (c) AHE after the subtraction of a linear slope. (d) Same as in (c) after smoothing.


492
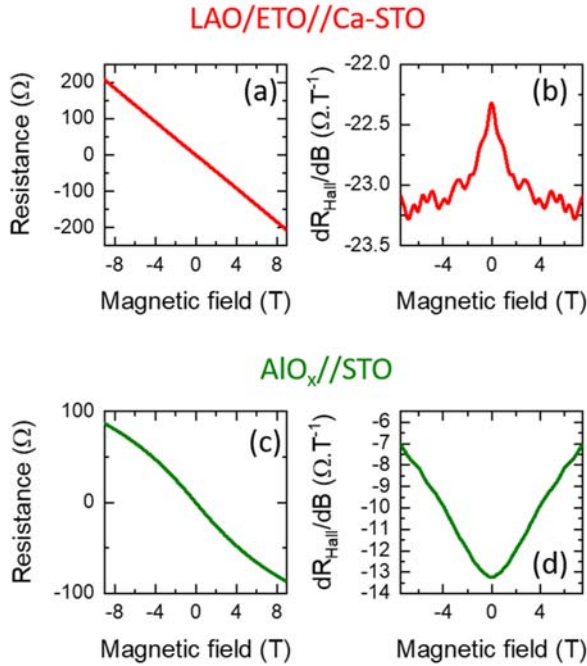
Extended data Fig. 6. Hall effect (a) and field derivative of the Hall effect (b) for a LAO/ETO//Ca-STO sample. Hall effect (c) and field derivative of the Hall effect (d) for a AlO$_x$//STO sample. The inverted-V

495 shape and V shape of the data in (b) and (d), respectively, indicate a non-linear component in the Hall
496 signal, but with a sign opposite in LAO/ETO//Ca-STO compared to AlOx//STO. While in AlOx//STO (and
497 in standard LAO/STO 2DEGs) this non-linearity is well explained by standard two-electronic bands
498 contributions, the non-linear component in LAO/ETO//Ca-STO has a different origin, only visible when
499 a magnetic layer is present[19], and thus ascribed to anomalous Hall effect.
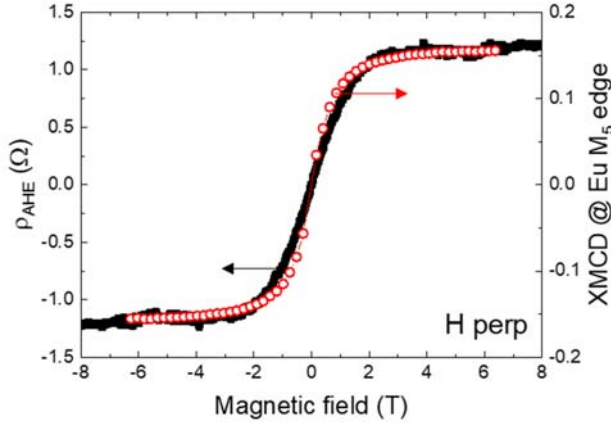
500

501 **Extended data Fig. 7.** Comparison of the field dependence of the AHE (left axis) and the XMCD at the
502 Eu M_5 edge (right axis), both measured at 2 K and with the magnetic field perpendicular to the plane.
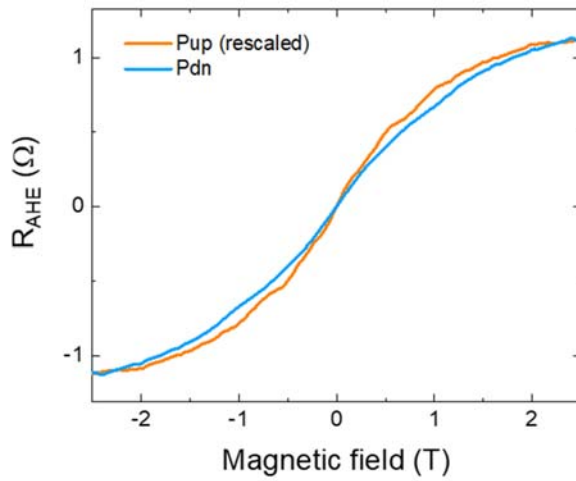
503

504 **Extended data Fig. 8.** Low magnetic field comparison of the AHE signal at 2 K for both remanent
505 polarization state, after rescaling the P_{up} signal to match the amplitude of the P_{dn} signal at high
506 magnetic field.